energies

MDPI

Article

Chemical Looping Reforming with Perovskite-Based Catalysts for Thermochemical Energy Storage

Stefano Padula [1], Claudio Tregambi [2,3], Maurizio Troiano [1,2], Almerinda Di Benedetto [1], Piero Salatino [1], Gianluca Landi [2,*] and Roberto Solimene [2,*]

[1] Dipartimento di Ingegneria Chimica, dei Materiali e della Produzione Industriale, Università degli Studi di Napoli Federico II, Piazzale Vincenzo Tecchio 80, 80125 Napoli, Italy
[2] Istituto di Scienze e Tecnologie per l'Energia e la Mobilità Sostenibili, Consiglio Nazionale delle Ricerche, Piazzale Vincenzo Tecchio 80, 80125 Napoli, Italy
[3] Dipartimento di Ingegneria, Università degli Studi del Sannio, Piazza Roma 21, 82100 Benevento, Italy
* Correspondence: gianluca.landi@stems.cnr.it (G.L.); roberto.solimene@cnr.it (R.S.)

Abstract: The performance of a perovskite-based oxygen carrier for the partial oxidation of methane in thermochemical energy storage applications has been investigated. A synthetic perovskite with formula $La_{0.6}Sr_{0.4}FeO_3$ has been scrutinized for Chemical Looping Reforming (CLR) of CH_4 under fixed-bed and fluidized-bed conditions. Temperature-programmed reduction and oxidation steps were carried out under fixed-bed conditions, together with isothermal reduction/oxidation cycles, to evaluate long-term perovskite performance. Under fluidized-bed conditions, isothermal reduction/oxidation cycles were carried out as well. Results obtained under fixed-bed and fluidized-bed conditions were compared in terms of oxygen carrier reactivity and stability. The oxygen carrier showed good reactivity and stability in the range 800–1000 °C. An overall yield of 0.6 Nm^3 of syngas per kg of perovskite can be reached per cycle. The decomposition of CH_4 catalyzed by the reduced oxide can also occur during the reduction step. However, deposited carbon is easily re-gasified through the Boudouard reaction, without affecting the reactivity of the material. Fluidized-bed tests showed higher conversion rates compared to fixed-bed conditions and allowed better control of CH_4 decomposition, with a H_2:CO ratio of around 2 and CO selectivity of around 0.8. However, particle attrition was observed and might be responsible for a loss of the inventory of up to 9%$_w$.

Keywords: fixed bed; fluidized bed; syngas; hydrogen; methane partial oxidation; isothermal cycles; concentrated solar thermal technologies

Citation: Padula, S.; Tregambi, C.; Troiano, M.; Di Benedetto, A.; Salatino, P.; Landi, G.; Solimene, R. Chemical Looping Reforming with Perovskite-Based Catalysts for Thermochemical Energy Storage. *Energies* **2022**, *15*, 8556. https://doi.org/10.3390/en15228556

Academic Editor: Andrea Frazzica

Received: 9 October 2022
Accepted: 9 November 2022
Published: 16 November 2022

1. Introduction

To fulfil the Paris Agreement, governments all around the world will have to sustain the transition toward sustainable technologies and enforce private companies to lower their carbon emissions. In this frame, renewable energies will steadily increase their share of the energy sector and thermal energy storage (TES) technologies can be very useful to integrating high shares of renewable energy in power generation, industry, and buildings. Clean energy sources such as solar, wind, and biomass have the additional advantages of being unlimited and distributed in every continent, which are relevant aspects also for energy security. The market of solar technologies has considerably grown in the past decade [1]. Concentrated Solar Thermal (CST) technologies use solar radiation as a heat source and today are exploited to supply steam power plants. A CST plant usually requires a field of heliostats to direct solar rays on a receiver. Despite large capital costs and land use, CST displays some promising features:

- exploitation of the whole solar spectrum, rather than a selected spectral range;
- simple integration with Thermal Energy Storage (TES) to allow continuous operation [1];
- smaller requirements for critical raw materials compared to competing technologies [2].

TES is recognized as a key technology to overcome solar inherent intermittency, to increase the dispatchability of solar energy, and to expand the applications of CST technologies. Several TES technologies have been proposed to be integrated with concentrated solar plants for power generation. They can be distinguished as: sensible, latent, and thermochemical energy storage. Sensible TES uses solid or liquid media to store thermal energy without changing their phase [3]. Currently, molten salts are generally used as the heat transfer and energy storage medium in sensible TES systems, but they are limited by a maximum operating temperature of 565 °C. Latent TES is based on the heat absorption or release when a storage material undergoes a phase change from solid to liquid or liquid to gas or vice versa. The main advantages of these systems rely on higher storage capacities at similar temperature range between charging and discharging steps. Several materials have been investigated and proposed to enhance heat transfer, such as inorganic salt-based phase-change materials, metallic alloys, and composites. Thermochemical Energy Storage (TCES) consists of exploiting available heat to drive an endothermic reaction. Solar energy is thus stored in the chemical products, rather than as sensible energy. The products can be stored for an unlimited time and can even be transported over large distances before being employed.

Several TCES processes are being developed. Most of them consist of chemical looping cycles, by which a solid material undergoes two or more reaction steps cyclically [4]. TCES may allow either the chemical storage/release of thermal energy for the generation of electricity or the production of sustainable fuels, chemicals, and materials. In the former case, the decomposition/recombination of metal hydrides, carbonates, hydroxides, and oxides is frequently considered [5]. In the latter case, the production of hydrogen (H_2), carbon monoxide (CO), or a mixture of them (synthesis gas) is pursued [6]. These gases can then be used to power gas turbines or fuel cells, or rather to produce advanced fuels and chemicals. Thermochemical splitting of water (H_2O) and carbon dioxide (CO_2) is an example: the endothermic step is the reduction of a metal oxide with the release of gaseous oxygen (O_2):

$$MO_x \rightarrow MO_{x-\delta} + \delta/2\ O_2, \quad (1)$$

The reduced oxide then reacts exothermically with H_2O and\or CO_2, producing H_2 and\or CO:

$$MO_{x-\delta} + \delta\ H_2O \rightarrow MO_x + \delta\ H_2, \quad (2)$$

$$MO_{x-\delta} + \delta\ CO_2 \rightarrow MO_x + \delta\ CO, \quad (3)$$

The reduced oxide allows splitting of H_2O or CO_2 at temperatures lower than through the direct homogeneous reaction. In addition, it works as an oxygen carrier: O_2 is released separately during the reduction step without mixing with the synthesis gas, and no explosive mixtures are formed. The reduction step typically requires temperatures of 1200–1500 °C and extremely low O_2 partial pressures, typically obtained by vacuum pumping or inert-gas sweeping. The introduction of a reducing agent allows more moderate thermodynamic conditions. If methane (CH_4) is used, the reaction temperature can be reduced [7]:

$$MO_x + \delta\ CH_4 \rightarrow MO_{x-\delta} + 2\delta\ H_2 + \delta\ CO, \quad (4)$$

The resulting overall reaction in this case is steam/dry reforming and the process is known as Chemical Looping Reforming (CLR). In principle, 4 moles of syngas can be produced from 1 mole of CH_4 per cycle, with a H_2:CO ratio that varies between 1 and 3 depending on whether CO_2 or H_2O is split during the oxidation step. The total energy content of the produced syngas is higher than the CH_4 feed by a factor U (upgrade factor) between 1.25 and 1.31, calculated as:

$$U = (n_{H2}\ LHV_{H2} + n_{CO}\ LHV_{CO})/(n_{CH4}\ LHV_{CH4}), \quad (5)$$

The selection of suitable metal oxides for thermochemical splitting is a wide research field [8,9]. The desired properties are:

- low reduction temperatures;
- high re-oxidation rates;
- high oxygen capacities (δ);
- good stability over cycles.

Volatile oxides release metal vapors when reduced. Zinc oxide (ZnO) falls into this category and has long been studied [10]. The efficient separation of the metal vapor from the product gas, to avoid recombination with O_2, is a fundamental aspect to consider [11]. The use of CH_4 [12] or carbon [13] as a reducing agent has been proposed for the combined production of Zn and synthesis gas. This shows how TCES can be integrated with other industrial sectors, opening to different markets. On the other side, non-volatile oxides have the advantage of remaining in a condensed state when reduced. Magnetite (Fe_3O_4) was the first oxide proposed for solar-driven thermochemical splitting and belongs to this category [14]. Mixed oxides have also been investigated as ferrites [15–17], aluminates [18], and perovskites [19], proving a higher stability during the high temperature reduction step. Despite limiting the oxygen capacity (δ), partial reduction to non-stoichiometric oxides shows beneficial aspects. Non-stoichiometric oxides preserve their crystal phase by letting oxygen diffuse through their lattice through the formation of vacancies. Among the advantages are moderate reduction temperatures, fast kinetics of re-oxidation, and good stability. Ceria (CeO_2) is a reference material of this kind [20]. The use of dopants enhances the stability of lattice defects and yields higher reduction degrees [21,22]. Perovskites are also non-stoichiometric oxygen carriers [19]. They are characterized by the presence of two cations and represented with the general formula ABO_3. Partial substitution of the A and B cations can be used to tailor the redox properties [23]. A Mars–van Krevelen-type reaction mechanism has been suggested for CLR [7,24,25]: adsorbed CH_4 reacts with lattice oxygen on the catalyst surface. The diffusion rate of bulk oxygen through the lattice dictates the selectivity of the process between partial and total oxidation products. Lanthanum (La)–iron (Fe) and La–manganese (Mn) perovskites have been found well-suited to CLR thanks to their high selectivity toward syngas (reaction (4)) [26,27]. La-substituted perovskites have been also investigated to enhance the mobility of oxygen and decrease C deposition. $La_{1-x}Sr_xFeO_3$ and $La_{1-x}Sr_xMnO_3$ perovskites were investigated in fixed-bed and membrane reactors [28,29], while a specific perovskite, $La_{0.85}Sr_{0.15}FeO_3$, was investigated in a fluidized-bed reactor [30]. Results were promising in terms of perovskite reactivity, partial oxidation of CH_4, and H_2O/CO_2 splitting, especially under fluidization conditions. However, only few studies are available in the literature on the use of $La_{1-x}Sr_xFeO_3$ perovskites under different reactor configurations, stimulating further research on the topic.

As TCES usually involves heterogeneous gas–solid reactions, the design of multiphase reactor technologies is fundamental for the development of these processes, and several examples are found in the literature [31]. Packed bed or porous solid structured reactors have been studied in the literature, with interesting results [32–35]. They benefit from low costs and easy operability, as they do not require the handling of the solids. However, poor mass transfer and temperature gradients due to nonuniform heating may limit the scale-up of these systems. Conventional and unconventional fluidized beds have been proposed for solar applications and have been recently reviewed [36]. Spouted [37] and internally circulating fluidized beds [38] have been studied under direct concentrated radiation to achieve uniform heating of the particles. Many authors have proposed concentration of solar radiation on the tube walls of fluidized beds [39], exploiting their large heat transfer coefficients. A pair of twin indirectly irradiated fluidized beds have been recently tested for thermochemical splitting with hercynite particles [39]. Dense circulating systems have been developed, both with up- [40] and down-flowing particle suspensions [41], to have a continuous operation. The recovery of the sensible energy of the outlet solid stream to preheat the inlet solid in a countercurrent heat exchanger has been studied both experimentally [42,43] and through modeling [44]. Finally, a multistage solar reactor, composed of multiple adjacent fluidized beds connected in series, has been recently proposed to

narrow the residence time distribution of the solid phase [45]. Fluidized beds have higher operating costs due to the pumping of the fluidizing gas and solid attrition and erosion, resulting in losses of inventory and wear of the equipment. However, a breakeven point can probably be reached, considering the undiscussed advantages of optimal temperature control, enhanced mass transfer, and better scalability.

This study investigates the redox properties of a laboratory-prepared perovskite for CLR of CH_4 in terms of reaction temperatures, oxygen capacity, and selectivity. A La-Sr-Fe-O system, specifically $La_{0.6}Sr_{0.4}FeO_3$, is tested as an oxygen carrier for the first time both in fixed-bed and fluidized-bed conditions. For this purpose, the time-resolved concentration profiles of the outlet gas were analyzed during reduction and oxidation steps. Oxidation was carried out with either H_2O or CO_2. The effect of temperature on reaction times has been qualitatively discussed with reference to a Mars–van Krevelen reaction mechanism. The material stability has been assessed by determining conversion degrees over iterated cycles. A critical comparison between fixed- and fluidized-bed performance in terms of reaction times and control of selectivity has been performed, to scrutinize the effect of gas–solid contact patterns.

2. Materials and Methods

2.1. Oxygen Carrier

The perovskite material was synthetized following the procedure developed in a previous study [23], to obtain a perovskite powder with chemical formula $La_{0.6}Sr_{0.4}FeO_3$. Briefly, stoichiometric amounts of strontium nitrate, lanthanum nitrate hydrate, and iron (III) nitrate nonahydrate (Sigma-Aldrich, St. Louis, MO, USA) were dissolved in 75 mL bi-distilled water and stirred for 3 h. The obtained solution was heated for about 10 min in a microwave oven (CEM SAM-155) up to the formation of a homogeneous gel, which was further calcined at 1100 °C for 4 h (heating rate: 10 °C/min). The powder was pressed into small cylindrical pads (2–3 mm diameter and height) with a bench-top press at 10 ton. Eventually, the pads were crushed into a mortar, and the fragments sieved in the size range 200–400 μm. Larger particles were crushed again, while finer particles were pressed again into pads, until granulation of the whole powder sample within the desired size range.

2.2. Experiments under Fixed-Bed Conditions

Figure 1 shows the set-up for the experiments under fixed-bed conditions. A perovskite sample (0.5 g) was placed on a porous plate inside a tubular quartz reactor with an internal diameter of 10 mm and heated by a cylindrical electric furnace (Lenton). A thermocouple, sheathed with a 6 mm tube, was vertically plunged into the sample along the center line of the reactor. A PID-type controller was used to set a heating rate or a fixed temperature. The reactants were diluted in a nitrogen (N_2) flow and fed at the top of the reactor. The gaseous species were fed from pure-gas cylinders through mass flow controllers (Brooks 5850S). Water was fed with a pump (Dionex P680 HPLC Pump) and vaporized by heating at 120 °C. A pressure transducer monitored the pressure upstream of the reactor inlet for safety reasons. The outlet gaseous stream was analyzed with two gas analyzers in series (Gas 3100 Syngas Analyzer and NGA 2000 from Rosemount) to detect the main chemical species (CH_4, CO, CO_2, H_2, O_2), after drying in a $CaCl_2$ trap. The reactor can be by-passed using a four-way valve to allow analysis of the feed.

The following experiments were run:

- Temperature-Programmed Reduction (TPR) from 25 to 1000 °C at 10 °C/min with CH_4
- Temperature-Programmed Oxidation (TPO) from 550 to 1000 °C at 10 °C/min with CO_2
- Isothermal cycles with CO_2 as oxidizer at 860, 920, and 1000 °C
- Isothermal cycles with H_2O as oxidizer at 920 °C

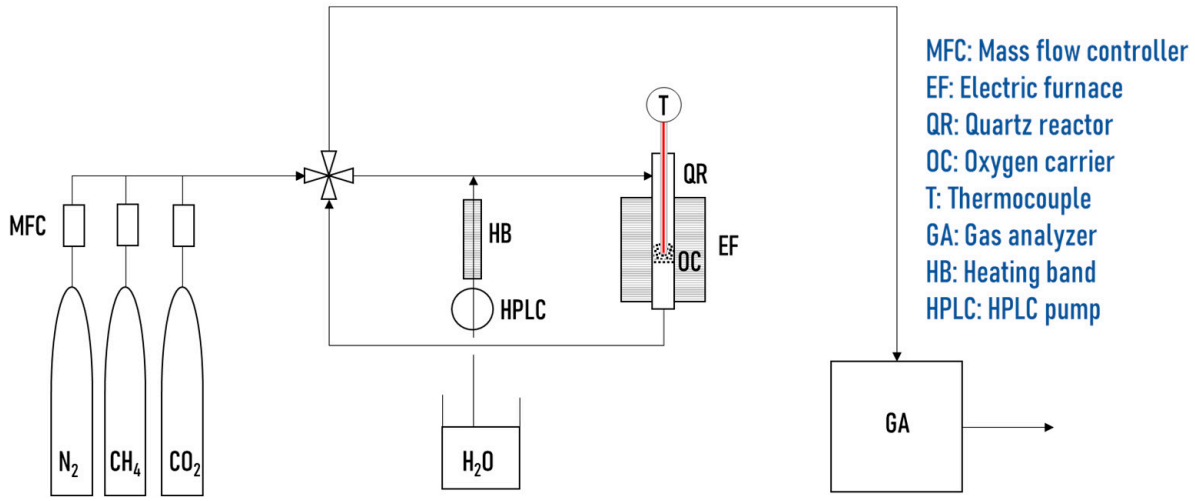

Figure 1. Experimental set-up for fixed-bed reaction tests.

For every test, the gas was fed from the top with a total flowrate of 10 NL/h, corresponding to a gas velocity between 0.14 and 0.17 m/s for the operating temperature range (860–1000 °C). The gas composition was 5% CH_4 for the reduction steps and 5% CO_2 for the oxidation steps. The concentration of H_2O could not be measured, but the pump was set to supply the oxidizer at the same concentration. A pure N_2 flow was used to sweep the reactor between consecutive reaction steps. After the TPO with CO_2, a TPO was performed with O_2 to ensure the full re-oxidation of the catalyst and to eventually burn unconverted coke deposited on the perovskite surface.

2.3. Experiments under Fluidized-Bed Conditions

The set-up for the experiments under fluidized-bed conditions was very similar (Figure 2). The perovskite sample (3.2 g), sieved in the range 250–355 µm, was placed in a tubular quartz reactor with an internal diameter of 10 mm inside a cylindrical electric furnace (Watlow Italy, Corsico (MI), Italy). The temperature of the catalyst was controlled with a PID controller. The fluidizing and reacting gases were fed from gas cylinders through mass flow controllers (Bronkhorst High-Tech B.V., Ruurlo, The Netherlands). The outlet gas passed through a bubble flowmeter, a water condenser, and finally through a gas analyzer (ABB, Advance Optima AO2020).

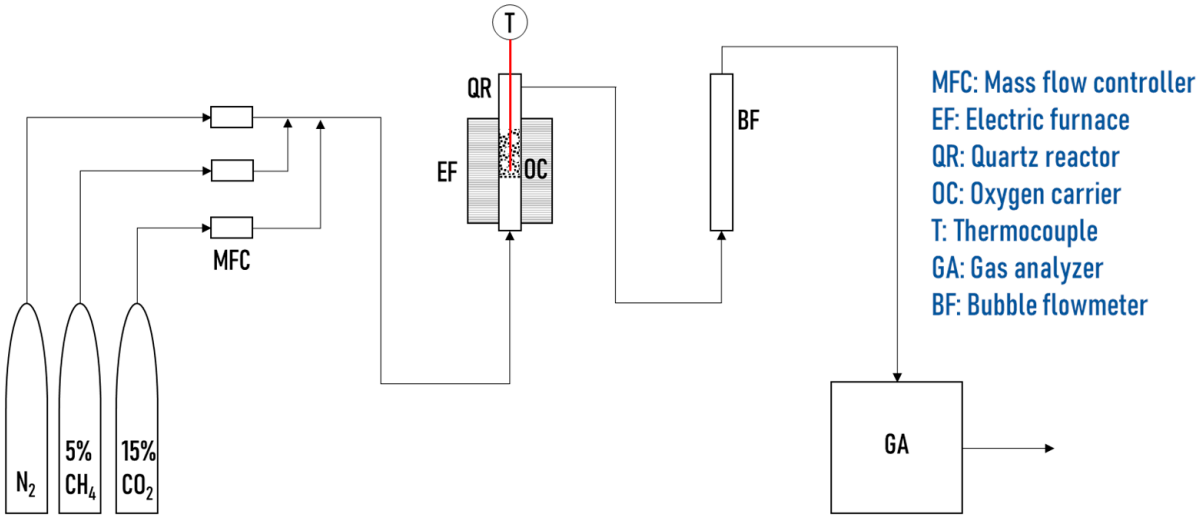

Figure 2. Experimental set-up for fluidized-bed reaction tests.

Similarly, for fixed-bed experiments, different tests were performed within the fluidized-bed reactor by varying the temperature and gas composition, to perform either the reduction or the oxidation step of the process. Isothermal cycles were conducted at 900 °C using CO_2 as oxidizer. A single long reduction step at 970 °C was conducted to study the decomposition of CH_4, followed by an oxidation step at 855 °C. The gas was fed from the bottom with a total flowrate of 70 NL/h, in order to have about the same contact time of the fixed-bed experiments. The corresponding fluidization velocity was about 1.1 m/s at 900 °C. The gas composition was 5% CH_4 for all the reduction steps, 15% CO_2 for the oxidation steps at 900 °C, and 8% CO_2 for the oxidation step at 855 °C.

3. Results and Discussion

3.1. Fixed-Bed Experiments

Figure 3 shows the temperature and concentration profiles from the TPR experiments. At about 800 °C, the reaction starts to take place with a high selectivity toward the products of partial oxidation and with a limited conversion of CH_4, as inferred from the H_2:CO concentration ratio of about 2. These observations suggest that the reaction is kinetically controlled by oxygen diffusion through the lattice of the perovskite, and as a consequence the concentration of oxygen on the surface of the catalyst is very low. A very little amount of CO_2 appears to be produced according to the reaction:

$$MO_x + \delta/4\, CH_4 \rightarrow MO_{x-\delta} + \delta/2\, H_2O + \delta/4\, CO_2, \quad (6)$$

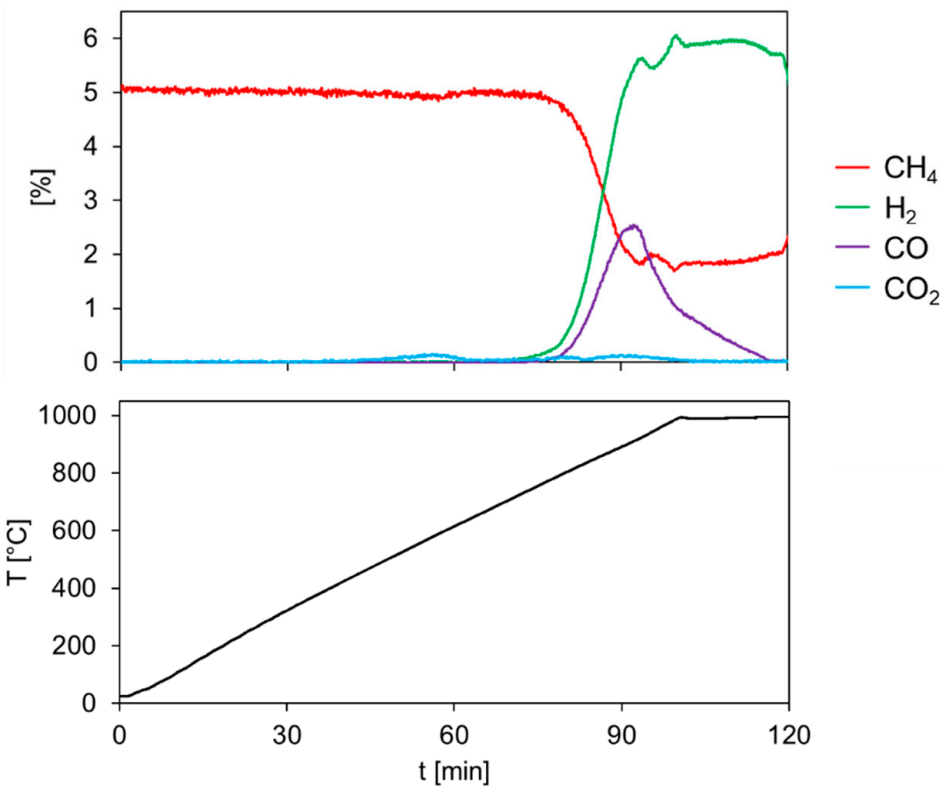

Figure 3. Temperature-Programmed Reduction with 5% CH_4 in fixed-bed conditions.

When the temperature exceeds 900 °C, the concentration of CO decreases but both the conversion of CH_4 and the production of H_2 continue. It is deduced that, as the catalyst is progressively reduced, CH_4 decomposition takes over, according to the reaction:

$$CH_4 \rightarrow C + 2\, H_2, \quad (7)$$

as confirmed by the ratio between the concentration of H_2 and that of consumed CH_4. The amount produced or reacted from each gaseous species can be calculated as follows:

$$n_i = N_{tot} \int | y_i^{in} - y_i^{out} | \, dt, \quad (8)$$

where N_{tot} is the total molar flowrate, and y_i^{in} and y_i^{out} are the inlet and outlet concentration of species i. From the atomic balances on hydrogen, carbon, and oxygen, it is possible to calculate the amount produced of H_2O and C and the amount of oxygen released by the perovskite:

$$4\, n_{CH4} = 2\, n_{H2} + 2\, n_{H2O}, \quad (9)$$

$$n_{CH4} = n_C + n_{CO} + n_{CO2}, \quad (10)$$

$$n_O = n_{CO} + 2\, n_{CO2} + n_{H2O}, \quad (11)$$

By dividing n_O by the moles of the sample ($n_{perovskite}$), it is observed that 1.5 moles of oxygen were released per mole of perovskite ($\delta = 1.5$), corresponding to the total reduction of iron from Fe^{+3} to Fe^0 and thus to the complete conversion of the oxygen carrier. The formation of Fe^0 may be responsible for the catalytic decomposition of CH_4 during the reduction step.

Figure 4 shows the temperature and concentration profiles during the TPO experiments. The reaction starts a little above the initial temperature of 550 °C, and above 800 °C the conversion of CO_2 is almost complete and then falls down as the catalyst is totally regenerated. The molar ratio between produced CO and converted CO_2 reaches values greater than unity, showing that gasification of deposited carbon according to the Boudouard reaction occurs simultaneously to perovskite oxidation, according to the reaction:

$$CO_2 + C \rightarrow 2\, CO, \quad (12)$$

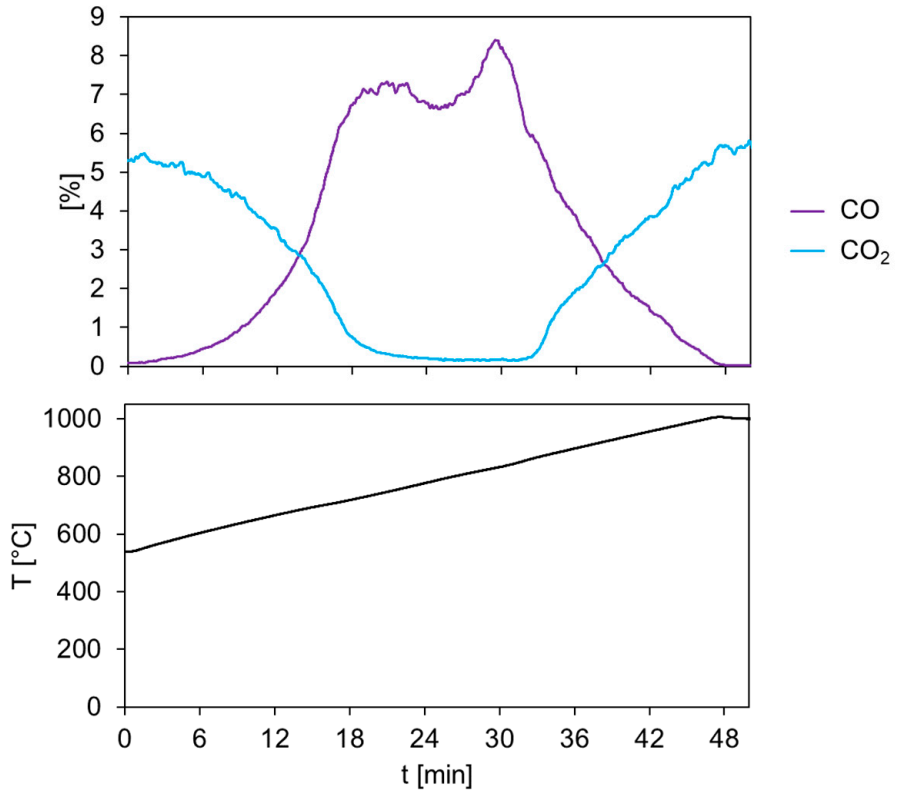

Figure 4. Temperature-Programmed Oxidation with 5% CO_2 in fixed-bed conditions.

The amounts involved in the reaction of the gaseous species can be calculated again from Equation (7). The atomic balances on carbon and oxygen give the amount of C re-gasified according to reaction (12) and the amount of oxygen uptaken by the perovskite:

$$n_C + n_{CO2} = n_{CO}, \quad (13)$$

$$2\, n_{CO2} = n_O + n_{CO}, \quad (14)$$

The calculations prove that the deposited carbon (C) is totally re-gasified according to reaction (12) and that the perovskite is completely re-oxidized. According to these results, a yield of 0.6 Nm^3 of syngas per kg of catalyst per cycle can be obtained from reactions (2–4), corresponding to the maximum value of $\delta = 1.5$. The value of δ and of syngas yield are in good agreement with the literature data on a similar perovskite [30].

Isothermal reaction profiles at different temperatures during the reduction steps are shown in Figure 5. During the course of the reaction, the selectivity toward CO decreases and the H_2:CO ratio increases, indicating that CH_4 thermocatalytic decomposition also occurs. The reduction steps were interrupted in order to limit the decomposition of CH_4 and the deposition of C on the catalyst. To this end, the concentration of CH_4, H_2, and CO were monitored and the feed of CH_4 was interrupted as soon as the selectivity toward CO appeared to drop below 80%. Except for an initial peak of CO_2, the favored products are H_2 and CO in every case and a quasi-steady condition is reached at 860 °C. These observations fit very well the interpretation of a fast reaction regime kinetically controlled by the diffusion of oxygen through the lattice sites: at the beginning of the reaction, CH_4 reacts with the oxygen-rich surface of the catalyst through complete oxidation; due to the low diffusion rate, the oxygen concentration at the surface rapidly drops down, approaching the minimum value allowed by the thermodynamic equilibrium. This is evident at 860 °C, as the gas composition probably mirrors an equilibrium condition. At higher temperatures, the reaction speeds up thanks to higher diffusivities and more favorable thermodynamic conditions, as witnessed by the concentration profiles. However, the reaction also slows down more rapidly, due to the faster reduction of the catalyst.

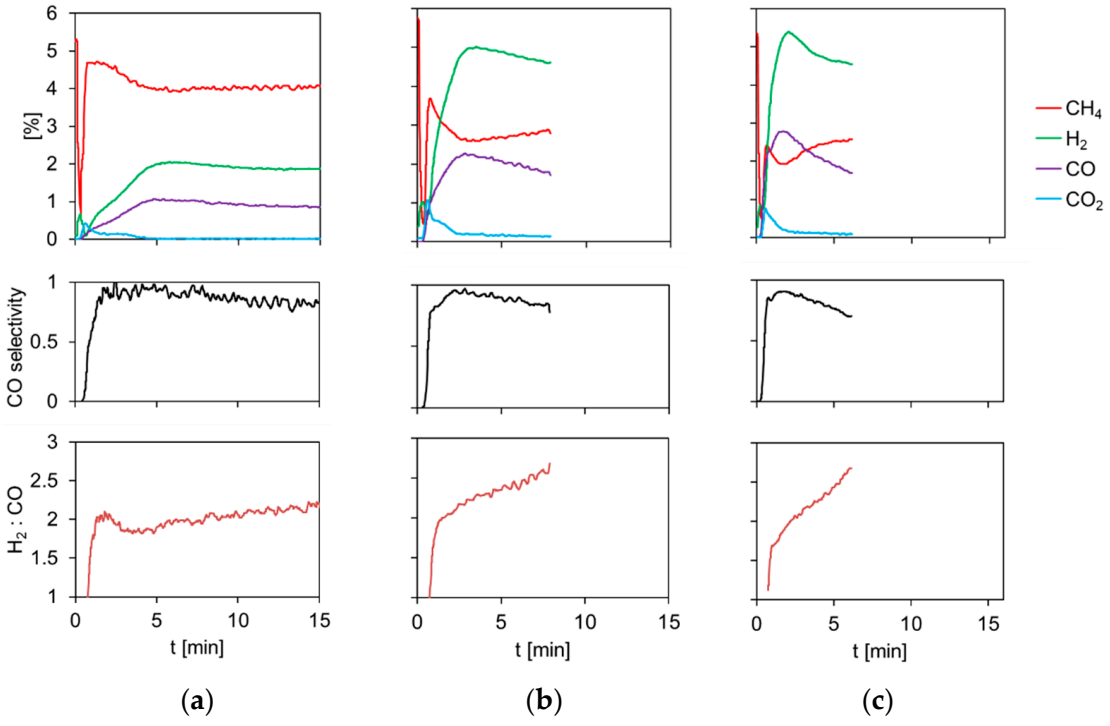

Figure 5. Reduction steps under fixed-bed conditions at 860 °C (**a**), 920 °C (**b**), 1000 °C, (**c**) with 5%.

In Figure 6, the isothermal oxidation steps are shown. The increase in temperature has opposite effects on the reaction rate. The initial peak of CO concentration indicates an increase in the kinetic rates of surface reactions. However, the reaction times do not increase monotonically. This can again be explained considering oxygen diffusion as the limiting step. At the beginning, the surface of the reaction is rapidly oxidized, producing the peak of CO, but it quickly saturates, reaching the highest oxygen concentration allowed by thermodynamics. Then, the reaction proceeds slowly, controlled by oxygen diffusion from the surface toward the bulk of the catalyst. As temperature is increased, the diffusivity also increases, and this can explain the reduction in the reaction time from 860 °C to 920 °C. However, at higher temperatures, unfavorable thermodynamic equilibrium limits the surface concentration of oxygen and thus slows the diffusion process. This might explain why the reaction time increases when raising the temperature from 920 °C to 1000 °C.

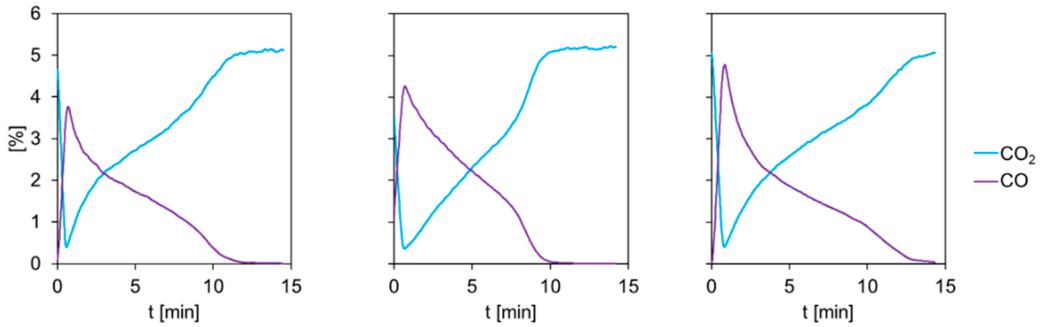

Figure 6. Oxidation steps under fixed-bed conditions at 860 °C (**a**), 920 °C (**b**), 1000 °C (**c**) with 5%.

Equations (8)–(11), (13) and (14) were solved for each of the isothermal cycles, and the conversion degrees of the sample were calculated as:

$$X = n_O/(1.5\ n_{perovskite}), \quad (15)$$

Figure 7 shows the results. A reduction degree around 50% and complete re-oxidation are observed for every process temperature. The cycles show good repeatability, and no deactivation trend is observed.

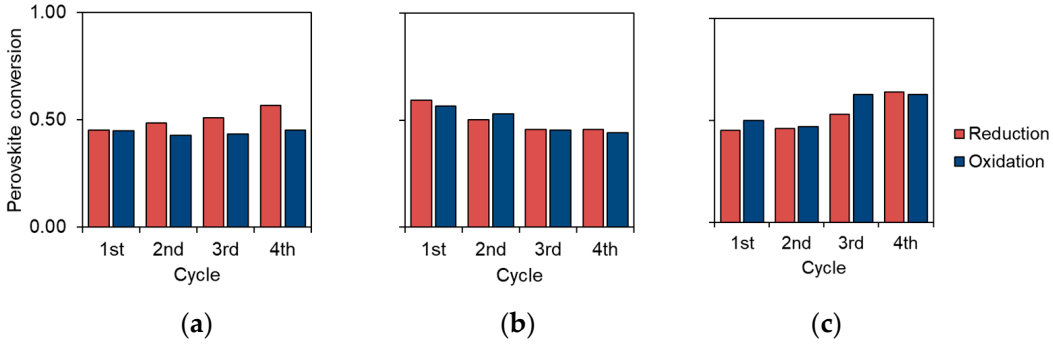

Figure 7. Conversion degree during reduction/oxidation isothermal cycles at (**a**) 860 °C, (**b**) 920 °C, (**c**) 1000 °C.

The results of the isothermal cycles at 920 °C using H_2O as oxidizer are shown in Figure 8. Six consecutive cycles were performed, using a shorter reaction time for the reduction step (6 min) to further limit CH_4 cracking. A reduction degree of about 40% was obtained. As for the CO_2 oxidation tests, the perovskite material showed complete re-oxidation and good cyclability.

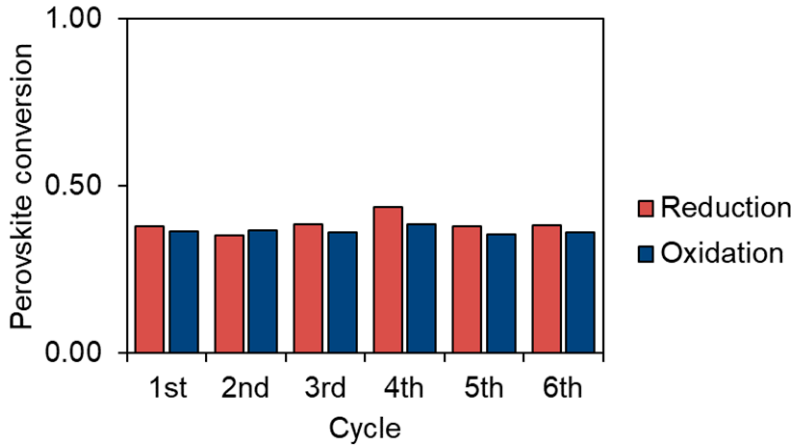

Figure 8. Conversion degree during reduction/oxidation isothermal cycles at 920 °C with H_2O.

3.2. Fluidized-Bed Experiments

Four isothermal cycles were conducted at 900 °C. During the first cycle the CH_4 feed was fed for 19 min to assess the time needed for the total reduction of the perovskite. For the following two cycles, the CH_4 feed was interrupted after 7 min to avoid CH_4 cracking and C deposition. Finally, the fourth cycle was carried on for 16 min to reach again full conversion of the perovskite. Figure 9 shows the reaction profiles of the second and fourth cycles. The reduction profiles (Figure 9a) show good repeatability. Total conversion of the perovskite is achieved in about 12 min and CH_4 decomposition initiates immediately after. The oxidation profiles (Figure 9b) differ for the Boudouard reaction, occurring in the fourth cycle.

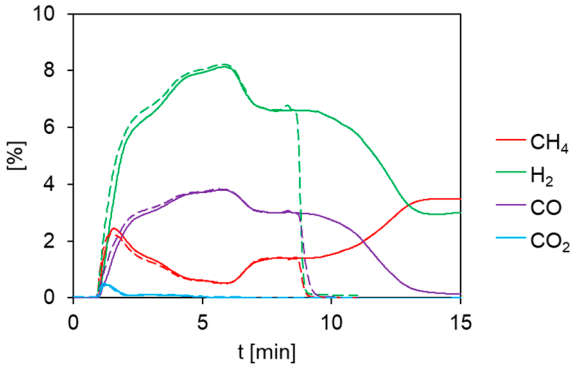

(**a**)

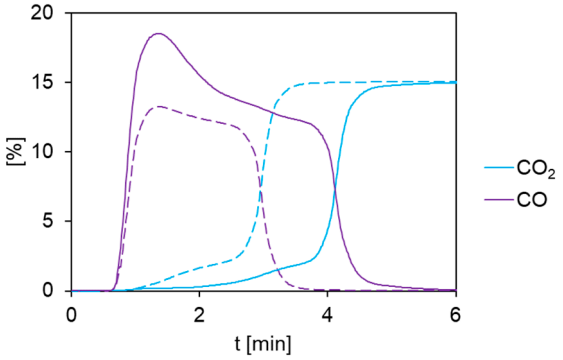

(**b**)

Figure 9. Isothermal cycles at 900 °C: reduction step (**a**), oxidation step (**b**), 2nd cycle (dashed line), 4th cycle (continuous line).

Figure 10 shows the perovskite conversion degrees. The reduction degree for 7 min at 900 °C was about 72%, whereas in fixed-bed experiments at 920 °C the reduction degree for about the same time was 50%, suggesting that, in fluidized-bed conditions, higher conversion rates can be obtained.

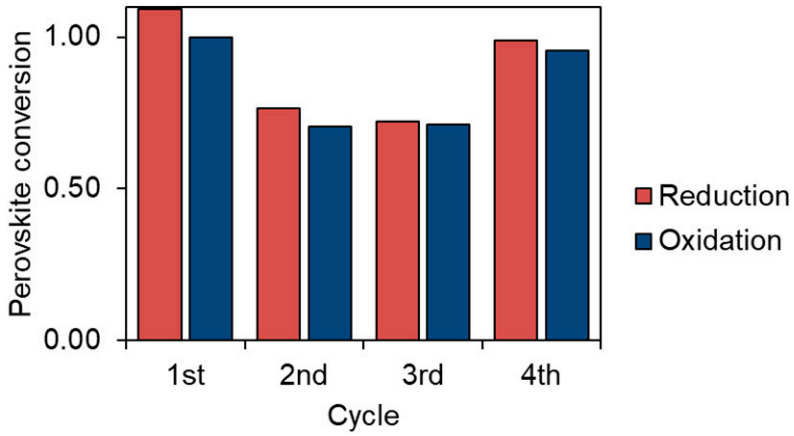

Figure 10. Isothermal cycles at 900 °C.

Finally, results of the long reduction test at 970 °C are shown in Figure 11. This test allowed investigation of the occurrence of deactivation phenomenon due to C deposition on the catalyst. Complete reduction of the perovskite is achieved in about 9 min. It can be pointed out that CH_4 is almost fully converted in this phase, showing again that the conversion rate is higher with respect to the case of the fixed bed (see Figure 5c). Then, CH_4 decomposition started and continued for more than 35 min. The decomposition rate showed a gradual but constant decrease, indicating an inhibiting effect of the deposited carbon. About 3 mmol of C was produced per mmol of catalyst, indicating that the reaction proceeds beyond the total coverage of catalytic Fe^0 sites.

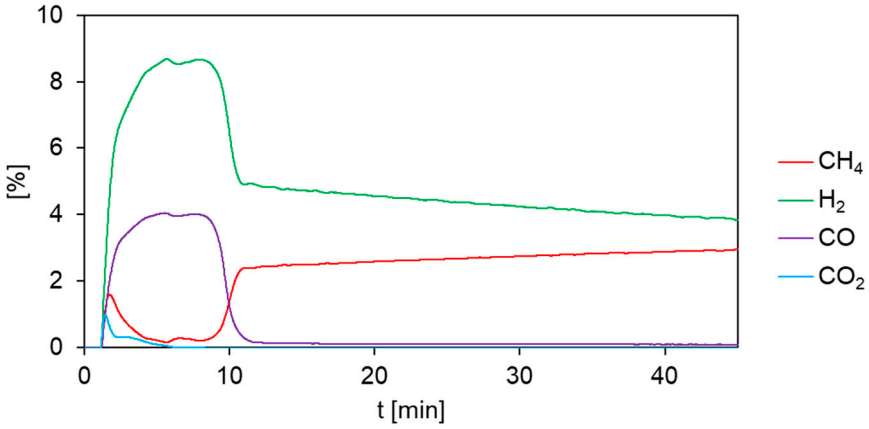

Figure 11. Perovskite reduction and CH_4 decomposition at 970 °C.

Figure 12 shows the profiles of the following regeneration step, performed at 855 °C with 8% CO_2. Again, complete regeneration of the catalyst could be achieved.

After the fluidized-bed tests, the perovskite sample was recovered, weighted, and sieved in order to assess eventual mass loss and particle size reduction. A 0.3 g amount of perovskite was found missing, and 0.1 g of the recovered perovskite had reduced its size below 250 μm. This indicates that the particles reduced their size by attrition and up to $9\%_w$ of the bed inventory might have been lost by elutriation.

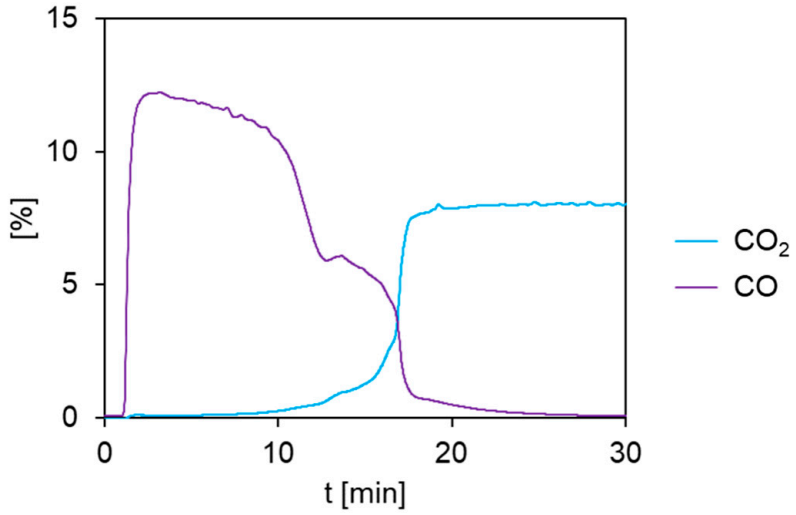

Figure 12. Catalyst regeneration at 855 °C.

3.3. Comparison between Fixed- and Fluidized-Bed Experiments

Finally, Figure 13 shows a comparison between the time profiles of the H_2:CO ratio, and the selectivity toward CO, for the reduction step at 1000 °C in fixed-bed conditions and the reduction step at 970 °C in fluidized-bed conditions. Under fluidized-bed conditions, CH_4 thermocatalytic decomposition initiates only at the end of the perovskite reduction, as inferred from the obtainment of a nearly constant H_2:CO ratio of 2 and selectivity of 0.8 throughout most of the experimental run. Differently, under fixed-bed conditions, the H_2:CO ratio soon exceeds the value of 2, with a concomitant decrease in the CO selectivity, indicating that CH_4 thermocatalytic decomposition starts much sooner and gradually takes over. This might be explained by the different contacting pattern between the gas reactant and the perovskite bed of particles. The fixed-bed conditions combined with the plug flow pattern of the gas phase determine that the layers of the catalyst at the inlet are reduced faster than those at the outlet. This leads to an early start of the decomposition reaction with respect to the complete reduction of catalyst particles. In fluidized-bed tests, instead, the solids perfect mixing conditions allow a uniform reduction degree of the particles, delaying CH_4 decomposition at the end of the bed solids reduction step.

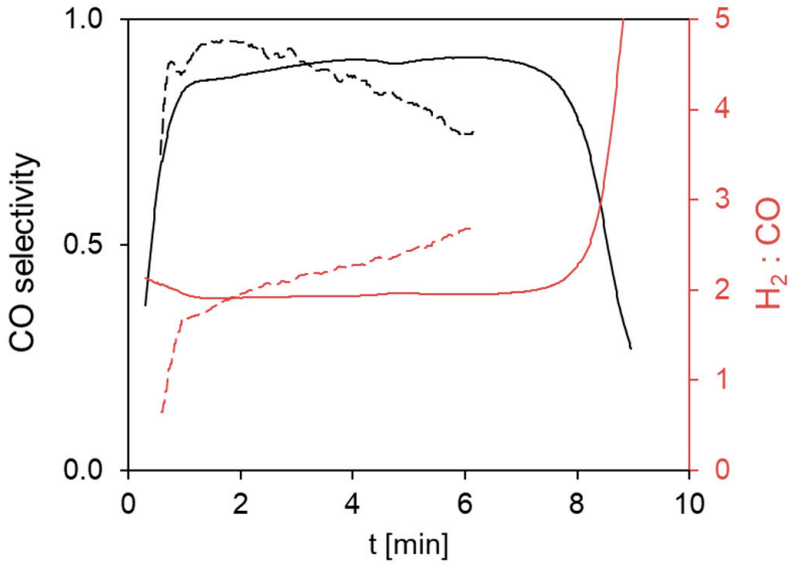

Figure 13. CO selectivity and H_2:CO ratio in fixed-bed conditions at 1000 °C (dashed line) and fluidized-bed conditions at 970 °C (continuous line).

4. Conclusions

A laboratory-produced perovskite catalyst has been tested in experiments of CLR of CH_4 under fixed- and fluidized-bed conditions. Temperature-programmed experiments indicate that the reduction can be performed at temperatures above 800 °C and the oxidation above 600 °C. Non-stoichiometric reduction yields a maximum value of $\delta = 1.5$, so 0.6 Nm^3 of syngas per kg of catalyst per cycle can be obtained from reactions (2–4). Except for a brief initial stage of the reduction, when the catalyst surface is rich of oxygen, the reaction evolves with a selectivity toward synthesis gas around 90%. Thermocatalytic decomposition of CH_4 catalyzed by the reduced oxide can occur during the reduction step. This drawback can be limited by interrupting the reduction step. C deposition does not deactivate the oxygen carrier, which is fully regenerated during the oxidation step thanks to gasification reactions. The overall H_2:CO ratio can be adjusted between 1 and 3, depending on whether CO_2 or H_2O is split during the oxidation step. CH_4 decomposition provides an additional degree of freedom to tune the H_2:CO ratio during the reduction step. No sign of a loss of reactivity was evidenced by determining the perovskite conversion degrees for several cycles at different temperatures. The reduction times decrease with temperature, whereas the oxidation times have a non-monotonical trend. Fluidized-bed tests showed higher conversion rates compared to fixed-bed conditions and allowed better control of CH_4 thermocatalytic decomposition. However, particle attrition was observed and might be responsible for a loss of the inventory of up to $9\%_w$. An improvement of the mechanical properties of the catalyst is an important issue to be addressed for scaled-up applications in fluidized beds. On the other hand, these results are very promising and provide a basis for the selection of operative conditions and reactor design, by considering the effect of temperature, reaction times, and gas–solid contact patterns.

Author Contributions: S.P.: conceptualization, formal analysis, investigation, methodology, visualization, writing—original draft. C.T.: conceptualization, methodology, writing—review and editing. M.T.: conceptualization, methodology, writing—review and editing. A.D.B.: conceptualization, methodology, supervision, writing—review and editing. P.S.: conceptualization, methodology, supervision, writing—review and editing. G.L.: conceptualization, methodology, supervision, writing—review and editing. R.S.: conceptualization, methodology, supervision, writing—review and editing. All authors have read and agreed to the published version of the manuscript.

Funding: This research received no external funding.

Data Availability Statement: Not applicable.

Conflicts of Interest: The authors declare no conflict of interest.

References

1. Gil, A.; Medrano, M.; Martorell, I.; Lazaro, A.; Dolado, P.; Zalba, B.; Cabeza, L.F. State of the Art on High Temperature Thermal Energy Storage for Power Generation. Part 1—Concepts, Materials and Modellization. *Renew. Sustain. Energy Rev.* **2010**, *14*, 31–55. [CrossRef]
2. Valero, A.; Valero, A.; Calvo, G.; Ortego, A. Material Bottlenecks in the Future Development of Green Technologies. *Renew. Sustain. Energy Rev.* **2018**, *93*, 178–200. [CrossRef]
3. Sarbu, I.; Sebarchievici, C. A Comprehensive Review of Thermal Energy Storage. *Sustainability* **2018**, *10*, 191. [CrossRef]
4. André, L.; Abanades, S.; Flamant, G. Screening of Thermochemical Systems Based on Solid-Gas Reversible Reactions for High Temperature Solar Thermal Energy Storage. *Renew. Sustain. Energy Rev.* **2016**, *64*, 703–715. [CrossRef]
5. Carrillo, A.J.; González-Aguilar, J.; Romero, M.; Coronado, J.M. Solar Energy on Demand: A Review on High Temperature Thermochemical Heat Storage Systems and Materials. *Chem. Rev.* **2019**, *119*, 4777–4816. [CrossRef]
6. Agrafiotis, C.; Roeb, M.; Sattler, C. A Review on Solar Thermal Syngas Production via Redox Pair-Based Water/Carbon Dioxide Splitting Thermochemical Cycles. *Renew. Sustain. Energy Rev.* **2015**, *42*, 254–285. [CrossRef]
7. Krenzke, P.T.; Fosheim, J.R.; Davidson, J.H. Solar Fuels via Chemical-Looping Reforming. *Sol. Energy* **2017**, *156*, 48–72. [CrossRef]
8. Roeb, M.; Neises, M.; Monnerie, N.; Call, F.; Simon, H.; Sattler, C.; Schmücker, M.; Pitz-Paal, R. Materials-Related Aspects of Thermochemical Water and Carbon Dioxide Splitting: A Review. *Materials* **2012**, *5*, 2015–2054. [CrossRef]
9. Scheffe, J.R.; Steinfeld, A. Oxygen Exchange Materials for Solar Thermochemical Splitting of H_2O and CO_2: A Review. *Mater. Today* **2014**, *17*, 341–348. [CrossRef]
10. Steinfeld, A. Solar Hydrogen Production via a Two-Step Water-Splitting Thermochemical Cycle Based on Zn/ZnO Redox Reactions. *Int. J. Hydrogen Energy* **2002**, *27*, 611–619. [CrossRef]

11. Alxneit, I. Assessing the Feasibility of Separating a Stoichiometric Mixture of Zinc Vapor and Oxygen by a Fast Quench—Model Calculations. *Sol. Energy* **2008**, *82*, 959–964. [CrossRef]
12. Steinfeld, A.; Brack, M.; Meier, A.; Weidenkaff, A.; Wuillemin, D. A Solar Chemical Reactor for Co-Production of Zinc and Synthesis Gas. *Energy* **1998**, *23*, 803–814. [CrossRef]
13. Osinga, T.; Frommherz, U.; Steinfeld, A.; Wieckert, C. Experimental Investigation of the Solar Carbothermic Reduction of ZnO Using a Two-Cavity Solar Reactor. *J. Sol. Energy Eng.* **2004**, *126*, 633–637. [CrossRef]
14. Nakamura, T. Hydrogen Production from Water Utilizing Solar Heat at High Temperatures. *Sol. Energy* **1977**, *19*, 467–475. [CrossRef]
15. Ehrensberger, K.; Frei, A.; Kuhn, P.; Oswald, H.R.; Hug, P. Comparative Experimental Investigations of the Water-Splitting Reaction with Iron Oxide $Fe_{1-Y}O$ and Iron Manganese Oxides $(Fe_{1-X}Mnx)_{1-Y}O$. *Solid State Ionics* **1995**, *78*, 151–160. [CrossRef]
16. Tamaura, Y.; Kojima, N.; Hasegawa, N.; Inoue, M.; Uehara, R.; Gokon, N.; Kaneko, H. Stoichiometric Studies of H_2 Generation Reaction for $H_2O/Zn/Fe_3O_4$ System. *Int. J. Hydrogen Energy* **2001**, *26*, 917–922. [CrossRef]
17. Gokon, N.; Mataga, T.; Kondo, N.; Kodama, T. Thermochemical Two-Step Water Splitting by Internally Circulating Fluidized Bed of $NiFe_2O_4$ Particles: Successive Reaction of Thermal-Reduction and Water-Decomposition Steps. *Int. J. Hydrogen Energy* **2011**, *36*, 4757–4767. [CrossRef]
18. Muhich, C.L.; Ehrhart, B.D.; Witte, V.A.; Miller, S.L.; Coker, E.N.; Musgrave, C.B.; Weimer, A.W. Predicting the Solar Thermochemical Water Splitting Ability and Reaction Mechanism of Metal Oxides: A Case Study of the Hercynite Family of Water Splitting Cycles. *Energy Environ. Sci.* **2015**, *8*, 3687–3699. [CrossRef]
19. Scheffe, J.R.; Weibel, D.; Steinfeld, A. Lanthanum–Strontium–Manganese Perovskites as Redox Materials for Solar Thermochemical Splitting of H_2O and CO_2. *Energy Fuels* **2013**, *27*, 4250–4257. [CrossRef]
20. Panlener, R.J.; Garnier, J.E.; Blumenthal, R.N. A Thermodynamic Study of Nonstoichiometric Cerium Dioxide. *J. Phys. Chem. Solids* **1976**, *37*, 368–378. [CrossRef]
21. Scheffe, J.R.; Steinfeld, A. Thermodynamic Analysis of Cerium-Based Oxides for Solar Thermochemical Fuel Production. *Energy Fuels* **2012**, *26*, 1928–1936. [CrossRef]
22. Luciani, G.; Landi, G.; Imparato, C.; Vitiello, G.; Deorsola, F.A.; Di Benedetto, A.; Aronne, A. Improvement of Splitting Performance of $Ce_{0.75}Zr_{0.25}O_2$ Material: Tuning Bulk and Surface Properties by Hydrothermal Synthesis. *Int. J. Hydrogen Energy* **2019**, *44*, 17565–17577. [CrossRef]
23. Luciani, G.; Landi, G.; Aronne, A.; Di Benedetto, A. Partial Substitution of B Cation in $La_{0.6}Sr_{0.4}MnO_3$ Perovskites: A Promising Strategy to Improve the Redox Properties Useful for Solar Thermochemical Water and Carbon Dioxide Splitting. *Sol. Energy* **2018**, *171*, 1–7. [CrossRef]
24. Otsuka, K.; Wang, Y.; Sunada, E.; Yamanaka, I. Direct Partial Oxidation of Methane to Synthesis Gas by Cerium Oxide. *J. Catal.* **1998**, *175*, 152–160. [CrossRef]
25. Pantu, P.; Kim, K.; Gavalas, G.R. Methane Partial Oxidation on $Pt/CeO_2–ZrO_2$ in the Absence of Gaseous Oxygen. *Appl. Catal. A Gen.* **2000**, *193*, 203–214. [CrossRef]
26. Nalbandian, L.; Evdou, A.; Zaspalis, V. $La_{1-X}Sr_xMO_3$ (M = Mn, Fe) Perovskites as Materials for Thermochemical Hydrogen Production in Conventional and Membrane Reactors. *Int. J. Hydrogen Energy* **2009**, *34*, 7162–7172. [CrossRef]
27. Iftikhar, S.; Martin, W.; Gao, Y.; Yu, X.; Wang, I.; Wu, Z.; Li, F. $LaNi_xFe_{1-x}O_3$ as Flexible Oxygen or Carbon Carriers for Tunable Syngas Production and CO_2 Utilization. *Catal. Today* **2022**, *in Press*. [CrossRef]
28. Evdou, A.; Zaspalis, V.; Nalbandian, L. $La_{(1-x)}SrxMnO_{3-\delta}$ Perovskites as Redox Materials for the Production of High Purity Hydrogen. *Int. J. Hydrogen Energy* **2008**, *33*, 5554–5562. [CrossRef]
29. Evdou, A.; Zaspalis, V.; Nalbandian, L. $La_{1-X}Sr_xFeO_{3-\delta}$ Perovskites as Redox Materials for Application in a Membrane Reactor for Simultaneous Production of Pure Hydrogen and Synthesis Gas. *Fuel* **2010**, *89*, 1265–1273. [CrossRef]
30. Donat, F.; Xu, Y.; Müller, C.R. Combined Partial Oxidation of Methane to Synthesis Gas and Production of Hydrogen or Carbon Monoxide in a Fluidized Bed Using Lattice Oxygen. *Energy Technol.* **2020**, *8*, 1900655. [CrossRef]
31. Zsembinszki, G.; Sole, A.; Barreneche, C.; Prieto, C.; Fernández, A.I.; Cabeza, L.F. Review of Reactors with Potential Use in Thermochemical Energy Storage in Concentrated Solar Power Plants. *Energies* **2018**, *11*, 2358. [CrossRef]
32. Almendros-Ibáñez, J.A.; Fernández-Torrijos, M.; Díaz-Heras, M.; Belmonte, J.F.; Sobrino, C. A Review of Solar Thermal Energy Storage in Beds of Particles: Packed and Fluidized Beds. *Sol. Energy* **2019**, *192*, 193–237. [CrossRef]
33. Marxer, D.; Furler, P.; Scheffe, J.; Geerlings, H.; Falter, C.; Batteiger, V.; Sizmann, A.; Steinfeld, A. Demonstration of the Entire Production Chain to Renewable Kerosene via Solar Thermochemical Splitting of H_2O and CO_2. *Energy Fuels* **2015**, *29*, 3241–3250. [CrossRef]
34. Guene Lougou, B.; Shuai, Y.; Zhang, H.; Ahouannou, C.; Zhao, J.; Kounouhewa, B.B.; Tan, H. Thermochemical CO_2 Reduction over $NiFe_2O_4$@alumina Filled Reactor Heated by High-Flux Solar Simulator. *Energy* **2020**, *197*, 117267. [CrossRef]
35. Tescari, S.; Singh, A.; Agrafiotis, C.; de Oliveira, L.; Breuer, S.; Schlögl-Knothe, B.; Roeb, M.; Sattler, C. Experimental Evaluation of a Pilot-Scale Thermochemical Storage System for a Concentrated Solar Power Plant. *Appl. Energy* **2017**, *189*, 66–75. [CrossRef]
36. Tregambi, C.; Troiano, M.; Montagnaro, F.; Solimene, R.; Salatino, P. Fluidized Beds for Concentrated Solar Thermal Technologies—A Review. *Front. Energy Res.* **2021**, *9*, 618421. [CrossRef]
37. Chuayboon, S.; Abanades, S.; Rodat, S. Insights into the Influence of Biomass Feedstock Type, Particle Size and Feeding Rate on Thermochemical Performances of a Continuous Solar Gasification Reactor. *Renew. Energy* **2019**, *130*, 360–370. [CrossRef]

38. Gokon, N.; Kumaki, S.; Miyaguchi, Y.; Bellan, S.; Kodama, T.; Cho, H. Development of a 5kWth Internally Circulating Fluidized Bed Reactor Containing Quartz Sand for Continuously-Fed Coal-Coke Gasification and a Beam-down Solar Concentrating System. *Energy* **2019**, *166*, 1–16. [CrossRef]
39. Hoskins, A.L.; Millican, S.L.; Czernik, C.E.; Alshankiti, I.; Netter, J.C.; Wendelin, T.J.; Musgrave, C.B.; Weimer, A.W. Continuous On-Sun Solar Thermochemical Hydrogen Production via an Isothermal Redox Cycle. *Appl. Energy* **2019**, *249*, 368–376. [CrossRef]
40. Zhang, H.; Benoit, H.; Perez-Lopèz, I.; Flamant, G.; Tan, T.; Baeyens, J. High-Efficiency Solar Power Towers Using Particle Suspensions as Heat Carrier in the Receiver and in the Thermal Energy Storage. *Renew. Energy* **2017**, *111*, 438–446. [CrossRef]
41. Miller, D.C.; Pfutzner, C.J.; Jackson, G.S. Heat Transfer in Counterflow Fluidized Bed of Oxide Particles for Thermal Energy Storage. *Int. J. Heat Mass Transf.* **2018**, *126*, 730–745. [CrossRef]
42. Tregambi, C.; Bevilacqua, C.; Troiano, M.; Solimene, R.; Salatino, P. A Novel Autothermal Fluidized Bed Reactor for Concentrated Solar Thermal Applications. *Chem. Eng. J.* **2020**, *398*, 125702. [CrossRef]
43. Tregambi, C.; Padula, S.; Galbusieri, M.; Coppola, G.; Montagnaro, F.; Salatino, P.; Troiano, M.; Solimene, R. Directly Irradiated Fluidized Bed Reactor for Thermochemical Energy Storage and Solar Fuels Production. *Powder Technol.* **2020**, *366*, 460–469. [CrossRef]
44. Padula, S.; Tregambi, C.; Solimene, R.; Chirone, R.; Troiano, M.; Salatino, P. A Novel Fluidized Bed " Thermochemical Battery " for Energy Storage in Concentrated Solar Thermal Technologies. *Energy Convers. Manag.* **2021**, *236*, 113994. [CrossRef]
45. Kong, W.; Wang, B.; Baeyens, J.; Li, S.; Ke, H.; Tan, T.; Zhang, H. Solids Mixing in a Shallow Cross-Flow Bubbling Fluidized Bed. *Chem. Eng. Sci.* **2018**, *187*, 213–222. [CrossRef]